JCI The Journal of Clinical Investigation

Amendment history:
- Corrigendum (November 2013)

An anticancer C-Kit kinase inhibitor is reengineered to make it more active and less cardiotoxic

Ariel Fernández, Angela Sanguino, Zhenghong Peng, Eylem Ozturk, Jianping Chen, Alejandro Crespo, Sarah Wulf, Aleksander Shavrin, Chaoping Qin, Jianpeng Ma, Jonathan Trent, Yvonne Lin, Hee-Dong Han, Lingegowda S. Mangala, James A. Bankson, Juri Gelovani, Aller Samarel, William Bornmann, Anil K. Sood, Gabriel Lopez-Berestein

J Clin Invest. 2007;117(12):4044-4054. https://doi.org/10.1172/JCI32373.

Technical Advance

Targeting kinases is central to drug-based cancer therapy but remains challenging because the drugs often lack specificity, which may cause toxic side effects. Modulating side effects is difficult because kinases are evolutionarily and hence structurally related. The lack of specificity of the anticancer drug imatinib enables it to be used to treat chronic myeloid leukemia, where its target is the Bcr-Abl kinase, as well as a proportion of gastrointestinal stromal tumors (GISTs), where its target is the C-Kit kinase. However, imatinib also has cardiotoxic effects traceable to its impact on the C-Abl kinase. Motivated by this finding, we made a modification to imatinib that hampers Bcr-Abl inhibition; refocuses the impact on the C-Kit kinase; and promotes inhibition of an additional target, JNK, a change that is required to reinforce prevention of cardiotoxicity. We established the molecular blueprint for target discrimination in vitro using spectrophotometric and colorimetric assays and through a phage-displayed kinase screening library. We demonstrated controlled inhibitory impact on C-Kit kinase in human cell lines and established the therapeutic impact of the engineered compound in a novel GIST mouse model, revealing a marked reduction of cardiotoxicity. These findings identify […]

 Related Commentary, page 3650

An anticancer C-Kit kinase inhibitor is reengineered to make it more active and less cardiotoxic

Ariel Fernández,[1,2,3] Angela Sanguino,[3] Zhenghong Peng,[4] Eylem Ozturk,[3,5] Jianping Chen,[2] Alejandro Crespo,[1] Sarah Wulf,[1] Aleksander Shavrin,[4] Chaoping Qin,[6] Jianpeng Ma,[1,6,7] Jonathan Trent,[8] Yvonne Lin,[9] Hee-Dong Han,[9] Lingegowda S. Mangala,[9] James A. Bankson,[10] Juri Gelovani,[4] Allen Samarel,[11] William Bornmann,[4] Anil K. Sood,[9,12] and Gabriel Lopez-Berestein[3]

[1]Department of Bioengineering and [2]Applied Physics Division, Rice Quantum Institute, Rice University, Houston, Texas, USA. [3]Department of Experimental Therapeutics and [4]Department of Experimental Diagnostic Imaging, Chemistry Section, University of Texas MD Anderson Cancer Center, Houston, Texas, USA. [5]Department of Chemistry, Hacettepe University, Ankara, Turkey. [6]Graduate Program of Structural and Computational Biology and Molecular Biophysics and [7]Department of Biochemistry and Molecular Biology, Baylor College of Medicine, Houston, Texas, USA. [8]Division of Cancer Medicine, Department of Sarcoma Medical Oncology, [9]Department of Gynecologic Oncology, and [10]Department of Imaging Physics, University of Texas MD Anderson Cancer Center, Houston, Texas, USA. [11]Cardiovascular Institute, Loyola University Medical Center, Maywood, Illinois, USA. [12]Department of Cancer Biology, University of Texas MD Anderson Cancer Center, Houston, Texas, USA.

Targeting kinases is central to drug-based cancer therapy but remains challenging because the drugs often lack specificity, which may cause toxic side effects. Modulating side effects is difficult because kinases are evolutionarily and hence structurally related. The lack of specificity of the anticancer drug imatinib enables it to be used to treat chronic myeloid leukemia, where its target is the Bcr-Abl kinase, as well as a proportion of gastrointestinal stromal tumors (GISTs), where its target is the C-Kit kinase. However, imatinib also has cardiotoxic effects traceable to its impact on the C-Abl kinase. Motivated by this finding, we made a modification to imatinib that hampers Bcr-Abl inhibition; refocuses the impact on the C-Kit kinase; and promotes inhibition of an additional target, JNK, a change that is required to reinforce prevention of cardiotoxicity. We established the molecular blueprint for target discrimination in vitro using spectrophotometric and colorimetric assays and through a phage-displayed kinase screening library. We demonstrated controlled inhibitory impact on C-Kit kinase in human cell lines and established the therapeutic impact of the engineered compound in a novel GIST mouse model, revealing a marked reduction of cardiotoxicity. These findings identify the reengineered imatinib as an agent to treat GISTs with curbed side effects and reveal a bottom-up approach to control drug specificity.

Introduction

Protein kinases, the signal transducers of the cell, are paradigmatic targets for drug-based cancer therapy (1–13). However, their evolutionary — and hence structural — relatedness often leads to unforeseen cross-reactivities (13–16), now surfacing through the advent of high-throughput screening technologies (6). Although the relationship between specificity and anticancer activity remains nebulous, a lack of specificity often underlies toxic side effects as the inhibitory impact diffuses away from clinically relevant targets (5, 14). Unwanted side effects can even be traced to inhibitory impact on a primary target, as in the reported cardiotoxicity of imatinib (STI571; Gleevec), likely due to its impact on Bcr-Abl (15), the chimeric Abelson kinase target in the treatment of chronic myeloid leukemia (CML) (5, 7, 8). Here we report on a rational drug-redesign strategy to control and refocus the inhibitory impact guided by a structure-based target discriminator. Thus, using a novel design concept, we modified imatinib to significantly reduce its impact on Bcr-Abl, prima facie curbing cardiotoxicity, while retaining anticancer activity on other primary targets.

The rationally redirected molecular impact of the prototype is corroborated in vitro and validated through tumor-derived cell lines and in an animal model. Thus, by sculpting into the ligand the de-wetting differences across imatinib targets, we focused the inhibitory impact specifically on the C-Kit kinase, a target for gastrointestinal stromal tumor (GIST) (9–11), while suppressing Bcr-Abl inhibition and promoting JNK inhibition, as needed to reinforce the prevention of cardiotoxicity (15). The discriminating molecular design is reflected in selective anticancer activity on GIST cell lines and a GIST animal model, and a prima facie reduction of cardiotoxicity.

Results

Discriminatory ligand design by sculpting unique nonconserved dehydration propensities. To engineer the affinity discriminator for C-Kit, we compare the patterns of residence times of water molecules that solvate the aligned interfacial regions of PDB-reported imatinib targets Bcr-Abl (PDB.1FPU), C-Kit (PDB.1T46), and lymphocyte-specific tyrosine kinase (Lck; PDB.3LCK) (http://www.rcsb.org/pdb/home/home.do; Figure 1, A–C; additional details

Nonstandard abbreviations used: BNP, brain natriuretic peptide; CML, chronic myeloid leukemia; DMPC, 1,2-dimyristoyl-*sn*-glycero-3-phosphocholine; EF, ejection fraction; GIST, gastrointestinal stromal tumor; Lck, lymphocyte-specific tyrosine kinase; NRVM, neonatal rat ventricular myocyte; TMB, 3,3′,5,5′-tetramethylbenzidene.

Conflict of interest: The authors have declared that no conflict of interest exists.

Citation for this article: *J. Clin. Invest.* **117**:4044–4054 (2007). doi:10.1172/JCI32373.

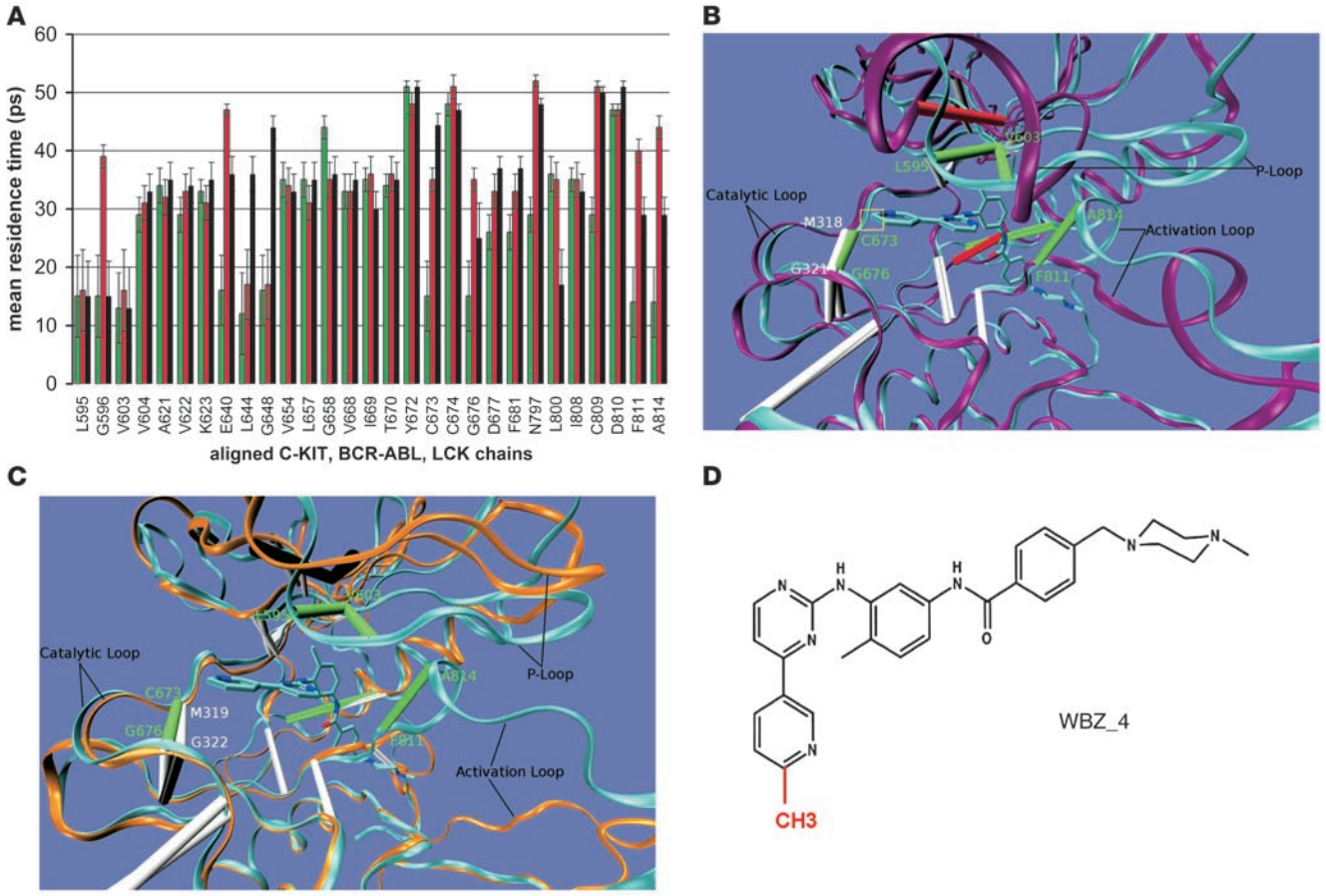

Figure 1

Comparison of de-wetting propensities of major imatinib targets and drug redesign dictated by de-wetting differences. (**A**) De-wetting propensities of C-Kit residues in contact with imatinib (PDB.1T46; green bars) and of aligned residues in Bcr-Abl kinase (PDB.1FPU; red bars) and Lck (PDB.3LCK; black bars). Residue *i* is in contact with the ligand if an atom of the latter lies within its domain, *D(i)* (see Methods). The de-wetting propensity is quantified by the mean residence time of solvating water molecules. Error bars denote Gaussian dispersion over 5 molecular dynamics runs. (**B**) Pattern of de-wetting hot spots that arise as backbone hydrogen-bonded residues in C-Kit kinase (ribbon backbone representation in light blue; de-wetting hot spots in green), aligned with Bcr-Abl kinase (magenta backbone; de-wetting hot spots in red). The imatinib methylation site leading to the expulsion of water from C-Kit C673-G676 de-wetting hot spot is highlighted (yellow rectangle). Imatinib is thus modified to favorably expel interfacial water molecules from the C-Kit microenvironment, a feature not conserved in Bcr-Abl. Hydrogen bonds are represented as segments joining α-carbons of the paired residues, and those lacking the propensity for dehydration are shown as light gray segments. Residues from the C-Kit chain are labeled in green, and those from Bcr-Abl are labeled in white. (**C**) Differences in de-wetting hot spots upon alignment of C-Kit (light blue backbone; hot spots in green) and Lck kinase (gold backbone; hot spots in black). Labels for Lck residues are shown in white. (**D**) Prototype molecule WBZ_4 (*N*-{5-[4-(4-methyl piperazine methyl)-benzoylamido]-2-methylphenyl}-4-[3-(4-methyl)-pyridyl]-2-pyrimidine amine). The added methyl group is indicated in red.

are provided in Supplemental Figure A.1–A.3; supplemental material available online with this article; doi:10.1172/JCI32373DS1). Hydrating molecules with low residence times (Figure 1A) constitute our blueprint for ligand reengineering, since they signal a local propensity for water removal. The crux of the redesign strategy is then the sculpting in the ligand of nonconserved local de-wetting propensities in the aligned targets: the ligand is engineered to remove interfacial water upon association according to weaknesses in the target hydration shell. Since this blueprint is typically not conserved across targets (Figure 1A) — although most surface residues in the binding region are — we can modulate the inhibitory impact of the compound to a certain extent. The key de-wetting hot spots correspond to amide-carbonyl backbone hydrogen bonds pairing backbone-exposed residues (13) (see Methods). Such bonds become energetically enhanced and stabilized upon removal of surrounding water and thus constitute de-wetting sites.

A de-wetting hot spot in C-Kit not conserved in the alternative targets is the residue pair C673-G676, which is mapped into the M318-G321 pair in Bcr-Abl and the M319-G322 pair in Lck (Figure 1, A–C). Thus, this local difference in de-wetting propensity prompted us to conceive and synthesize a methylated variant of imatinib, heretofore named WBZ_4 (synthesis described in Supplemental Data) (Figure 1D). Achieving a higher level of favorable and selective interactivity required an exogenous modulation of the target microenvironment, in turn requiring a modification of the parental compound. As dictated by the de-wetting blueprint (Figure 1, B and C), the added methyl group would promote the

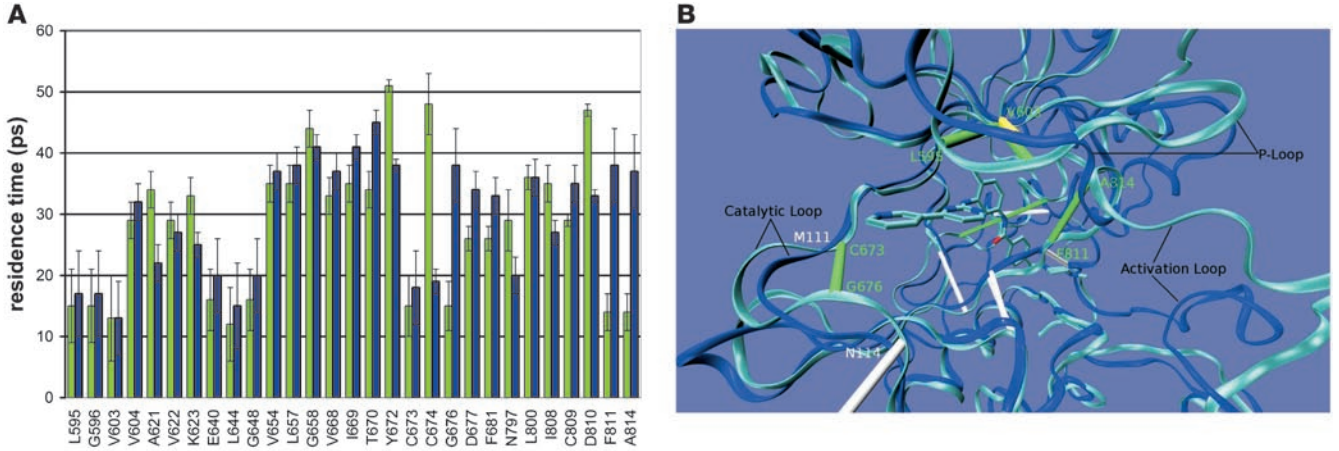

Figure 2
Comparison of de-wetting propensities of C-Kit and JNK. (**A**) Aligned de-wetting patterns for C-Kit kinase (green) and JNK1 (blue) restricted to the C-Kit residues in contact with imatinib. (**B**) De-wetting hot spots arising as backbone hydrogen-bonded residues in C-Kit kinase (backbone in light blue; de-wetting hot spots in green), aligned with JNK (blue backbone; de-wetting hot spots in yellow). The JNK residues M111 and N114, aligned with the de-wetting hot spot C673-G676 in C-Kit, are not paired by a hydrogen bond. Yet M111 is a de-wetting hot spot for JNK (Figure 1E), hence a harnessing spot for the designed imatinib modification.

favored dehydration of the pair C673-G676 upon binding to C-Kit, while it would hamper the association with Bcr-Abl and Lck, since the latter kinases favor hydration of the catalytic loop residues aligned with the targeted C-Kit residues C673-G676 (Figure 1A).

Reported assays on imatinib-triggered cardiomyocyte damage point to a beneficial JNK (JNK1) inhibition to reduce the induced collapse of mitochondrial membrane potential and preserve sarcolemmal integrity (15). For this reason, we tested the molecular harnessing of WBZ_4 on the de-wetting pattern of JNK1 (PDB.2G01). This analysis required alignment of JNK1 with the imatinib–C-Kit complex (PDB.1T46) (Figure 2, A and B). The high de-wetting propensity at JNK1 residue M111, the residue that aligns with C673 in C-Kit, instills confidence in the affinity of WBZ_4 for JNK.

Molecular dynamics analysis. We first probed WBZ_4 in silico by monitoring the spatiotemporal effect of the specific methylation on the kinase-inhibitor association through molecular dynamics (Figure 3, A and B). As C-Kit associates with imatinib, the loop facing the para-position on the terminal ring (Figure 1B and Figure 3A) was found to be unstable. In all 5 simulation trajectories, the backbone hydrogen bond between C673 and G676 was irreversibly replaced by water-mediated interactions within 1 ns (Figure 3A). When WBZ_4 replaced imatinib within the C-Kit complex, the same loop was found to be stabilized due to the improved dehydration of the hydrogen bond by the added methyl group on the ligand (Figure 3B). Thus, for C-Kit, WBZ_4 introduces favorable interactions engaging the solvent-exposed preformed hydrogen bond and consequently stabilizes the inhibitor binding. The effect of WBZ_4 is the opposite on Bcr-Abl. Our simulations demonstrate that, in this case, the imatinib complex has a better stability in the same loop region, while WBZ_4 significantly destabilizes the loop. This is due to the fact that the M318-G321 backbone hydrogen bond on the Bcr-Abl loop is well dehydrated intramo-

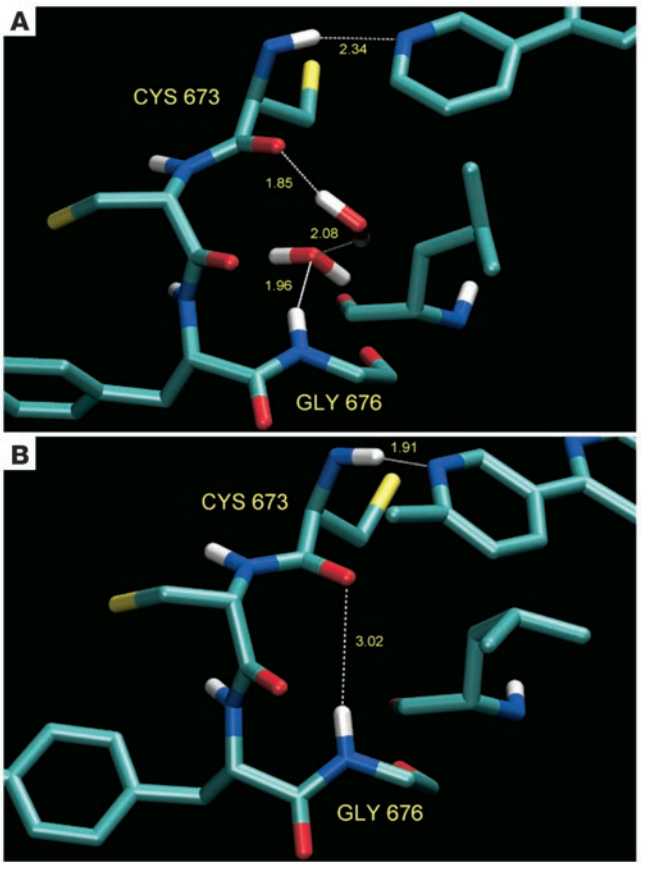

Figure 3
Water exclusion patterns promoted by imatinib and WBZ_4 on the primary target C-Kit. (**A**) Snapshot of the SBMD simulation for C-Kit kinase bound to imatinib at 1 ns. The main-chain hydrogen bond between C673 and G676 is competitively and irreversibly replaced by hydrogen bonding to a water molecule, revealing the instability of the intramolecular interaction. (**B**) Snapshot of the SBMD simulation of C-Kit kinase in complex with WBZ_4 at 1 ns. The main-chain hydrogen bond between C673 and G676 is stabilized by the water expulsion promoted by the added methyl on the inhibitor.

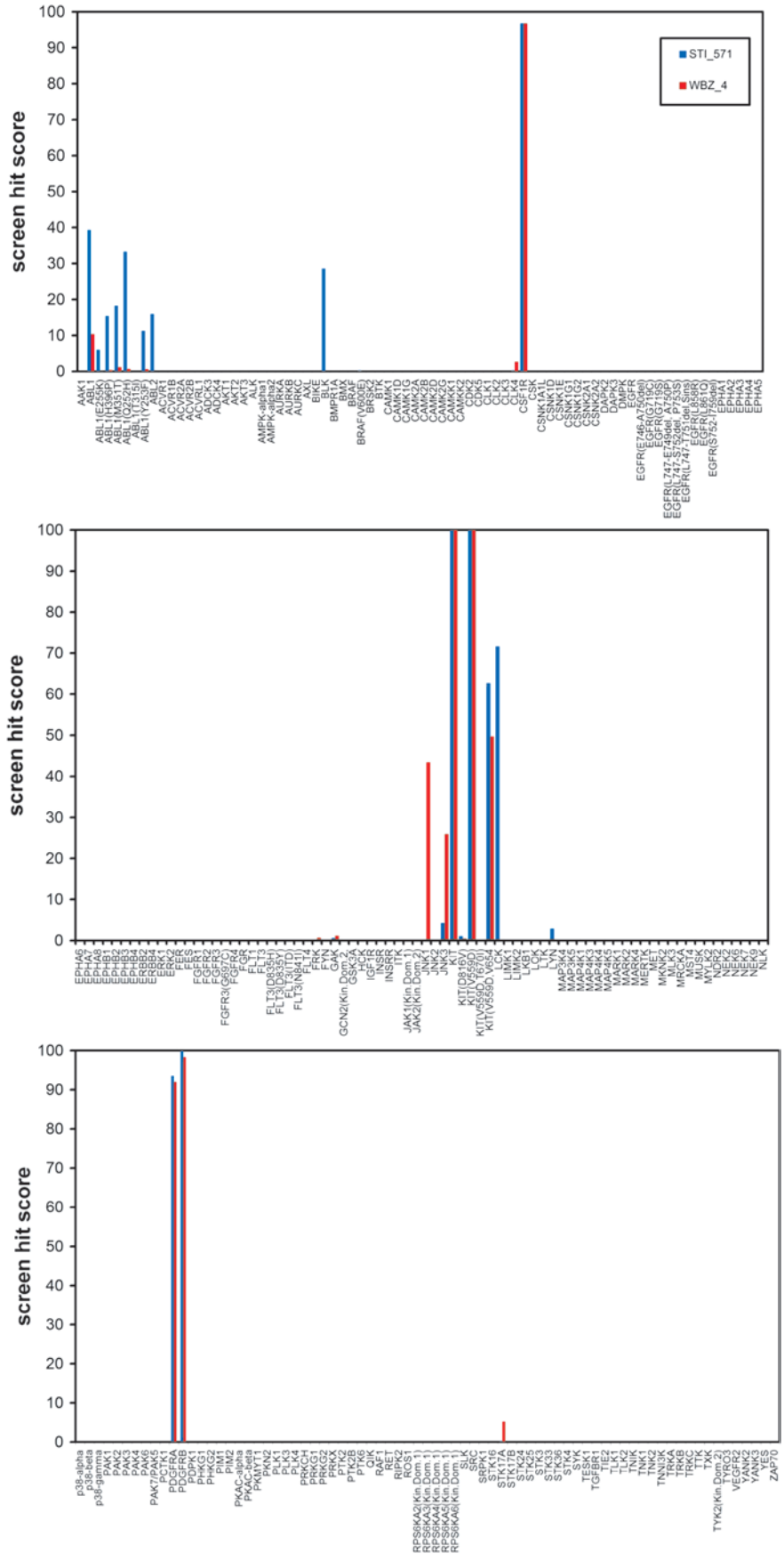

Figure 4
High-throughput screening at 10 mM for WBZ_4 (red) and imatinib (STI_571; blue; control) over a battery of 228 human kinases displayed in a T7-bacteriophage library (Ambit Biosciences). Hit values are reported as percentage bound kinase.

lecularly and positioned closer to imatinib; thus this bond becomes well protected (17) by imatinib, and the addition of the methyl group clashes sterically with the loop. Thus, molecular dynamics provides a convincing rationale for the discriminatory power of WBZ_4 relative to imatinib.

High-throughput screening: avoiding the c-Abl kinase while inhibiting JNK. To test our predictions, WBZ_4 was first screened for affinity against a T7-bacteriophage library displaying 228 human kinases (Ambit Biosciences) (6) (Figure 4), using imatinib screening as control. The selective affinity of WBZ_4 for C-Kit kinase and JNK1 is noteworthy. Predictably, the affinity of WBZ_4 for Abl1 is reduced by 75% and by 95% or more on all other Abl variants, while, in contrast with imatinib, WBZ_4 shows no detectable affinity for Lck. The impact of WBZ_4 on all additional imatinib targets was comparable, while its controlled specificity is apparent.

In vitro assays: assessing the expected modulation of inhibitory impact. The specificity of WBZ_4 toward C-Kit was established first through in vitro assays that dissect the kinetics of competitive inhibition (8, 18) independently of cancer cell circuitry (19–22). The inhibitory impact of imatinib (triangles) and WBZ_4 (squares) on the rate of phosphorylation was determined by spectrophotometry, assaying for the activity of C-Kit and Bcr-Abl (Figure 5, blue and red plots, respectively) (8). The assay couples production of ADP, the by-product of downstream phosphorylation, with the concurrent detectable oxidation of NADH. This oxidation results upon transfer of phosphate from phosphoenolpyruvate (PEP) to ADP, followed by the NADH-mediated reduction of PEP to lactate. Thus, substrate phosphorylation is monitored by the decrease in absorbance at 340 nm due to the oxidative conversion of NADH to NAD^+. These kinetic assays revealed a high specificity of WBZ_4 for C-Kit, in contrast with imatinib. WBZ_4 enhances the inhibition of C-Kit activity even beyond imatinib levels, revealing a higher competitive affinity of the prototype compound for the ATP-

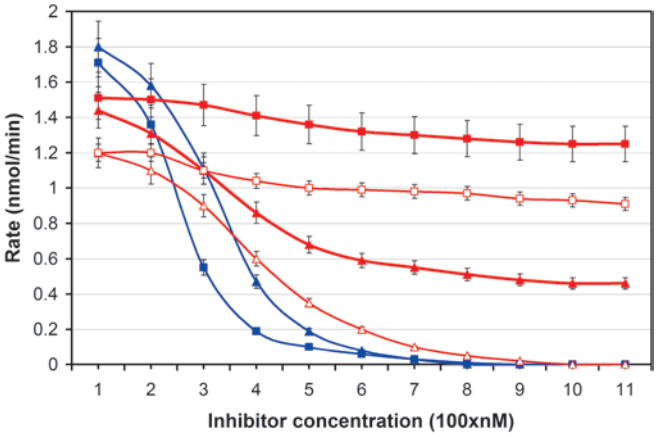

Figure 5
Kinetic inhibitory impact of compounds WBZ_4 and imatinib determined by measuring phosphorylation rates through spectrophotometric assays of C-Kit and Bcr-Abl kinase activity. The kinases are inhibited by WBZ_4 (squares) and by the parental compound (triangles). Phosphorylation rate plots are given for Bcr-Abl (red) and C-Kit (blue). The open red symbols correspond to inhibition of unphosphorylated Bcr-Abl, while the filled red symbols correspond to the Tyr412-phosphorylated form. Error bars represent dispersion over 5 runs for each kinetic assay.

binding pocket [K_I (imatinib) ≈ 55 ± 7 nM; K_I (WBZ_4) ≈ 43 ± 5 nM]. On the other hand, the pattern of inhibition for Bcr-Abl is dependent on the phosphorylation state of this kinase (20). At 1 μM concentration, imatinib reduces 66% of the activity of Tyr412-phosphorylated kinase (8) (K_I ≈ 5 ± 1 μM) and approximately 100% of the activity of the unphosphorylated state (K_I ≈ 50 ± 5 nM). By contrast, 1 μM WBZ_4 reduces by less than 20% the activity of both states of Bcr-Abl. The prototype compound has reciprocal affinity constants K_I ≈ 18 ± 3 μM and K_I ≈ 11 ± 2 μM for phosphorylated and unphosphorylated Bcr-Abl, respectively.

In vitro colorimetric assays were performed over a 1 pM to 100 μM range in ligand concentration to assess the inhibition of phosphorylating activity by antibody recognition of phosphorylated peptide substrates (see Methods). The IC_{50} (50% inhibition concentration) for imatinib/Abl is approximately 1 μM, while the WBZ_4/Abl value is greater than 100 μM (Figure 6A). The active recombinant Abl kinase and its substrate (Abl-tide) were incubated in the presence of various WBZ_4 or imatinib concentrations and ATP (100 nM). Phosphorylation of Abl-tide was detected by spectrophotometry following incubation with anti-rabbit phospho–Abl-tide antibody and subsequently with HRP antibody (see Methods).

The specificity of the inhibitory impact on C-Kit is significantly enhanced as WBZ_4 substitutes imatinib (Figure 6, A and B), while C-Kit inhibition is 23% ± 12% greater for WBZ_4 (Figure 6B). The impact of our prototype ligand on alternative imatinib targets, such as the PDGFR kinase, could not be modulated, since such proteins are not reported in PDB, and thus no de-wetting pattern can be reliably identified (compare high-throughput screening of WBZ_4 versus imatinib in Figure 4).

In vitro assays for selective anticancer activity. The controlled inhibitory impact was further tested through in vitro models. The initial decisive tests entailed treating the GIST882 (12) cell line and the CML K562 (7) cell line with WBZ_4 and contrasting its inhibitory impact on cell proliferation and in-cell specificity with

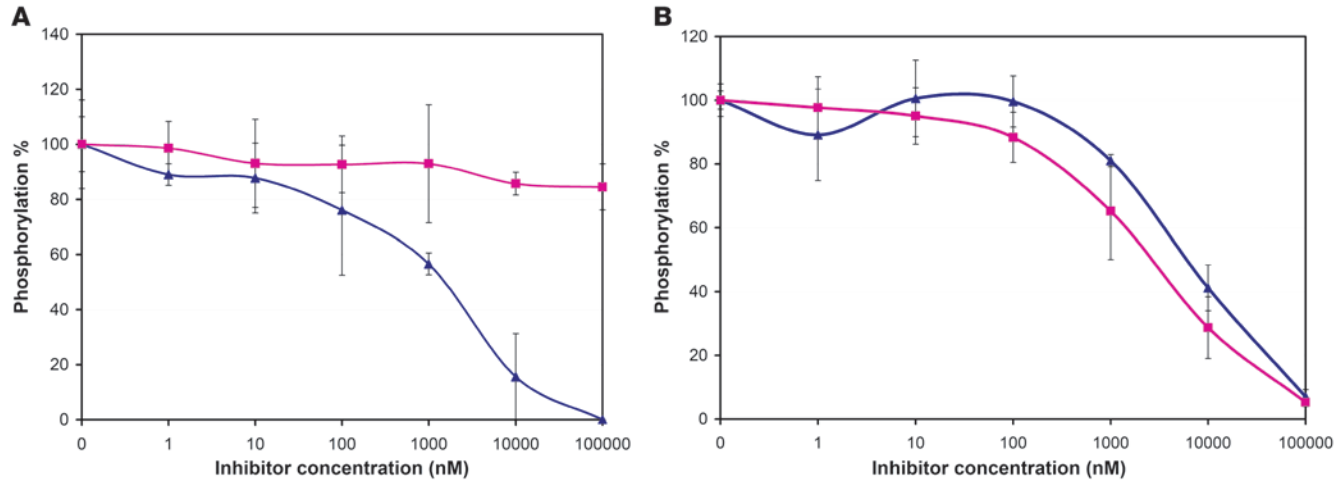

Figure 6
In vitro comparison of inhibitory impact of imatinib and WBZ_4 on Abl and C-Kit kinase. (**A**) In vitro phosphorylation inhibition assay for Abl enzyme in the presence of WBZ_4 (pink) or imatinib (blue). Active recombinant Abl enzyme (1 μg/ml) and its substrate (Abl-tide; 1 μg/ml) were incubated for 1 hour at 37°C in the presence of various WBZ_4 or imatinib concentrations. ATP (100 nM) was added to the reaction mixture. Phosphorylation of Abl-tide peptide was detected by incubation in consecutive order with anti-rabbit phospho–Abl-tide antibody and anti-rabbit HRP antibody. TMB was added to initiate the chromophore reaction, and 2 minutes were allowed for color development. The reaction was terminated by the addition of 1 M H_2SO_4. Phosphorylation of the substrate was quantified as absorbance units (AU) by spectrophotometry at 450 nm. Values obtained with the enzyme without the inhibitors (WBZ_4 or imatinib) were assumed to represent 100% phosphorylation and were compared with the values obtained with the addition of the inhibitors. (**B**) In vitro phosphorylation inhibition assay for C-Kit in the presence of WBZ_4 (pink) or imatinib (blue). Active recombinant C-Kit kinase (25 ng/ml) and its substrate Poly(Glu4-Tyr) (150 nM) were incubated for 1 hour at 37°C in the presence of various WBZ_4 or imatinib concentrations. ATP (100 nM) was added to the reaction mixture. Phosphorylation of Poly(Glu4-Tyr) peptide was detected by incubation in consecutive order with anti-phosphotyrosine antibody and anti-rabbit HRP antibody.

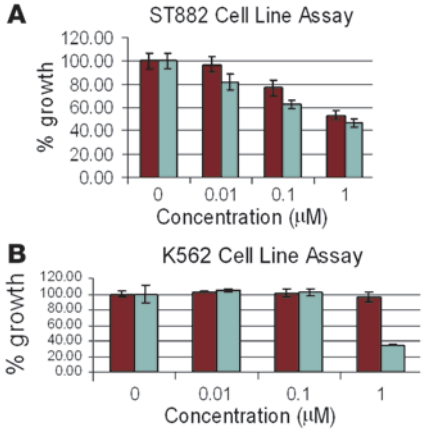

Figure 7
Comparison of inhibitory impact of imatinib and WBZ_4 on cell proliferation. (**A**) Cell proliferation assay for GIST882 cells. WBZ_4 inhibits cell proliferation of C-Kit–positive ST882 cells. GIST cancer cells ST882 (GIST882) were seeded in 96-well plates at a density of 8×10^3 cells per well. The cells were treated with various concentrations of WBZ_4 (red) and imatinib (light blue) for an additional 48 hours. Cell proliferation was determined by Alamar blue assay (see Methods). Cell proliferation is expressed as the percentage of proliferating cells relative to untreated cells. The WBZ_4 compound was incorporated into liposomes (see Methods) to facilitate cellular delivery. (**B**) Cell proliferation assay for K562 cells. WBZ_4 does not significantly inhibit cell proliferation of Bcr-Abl–expressing K562 cells. K562 cells were seeded in 96-well plates at a density of 1×10^4 cells per well in 50 μl of medium. Two hours later, 50 μl medium containing different concentrations (0.01, 0.1, 1 μM) of liposome-encapsulated WBZ_4 (red) or soluble imatinib (light blue) were added to the wells to reach a final volume of 100 μl per well. Following 48 hours of exposure, the Alamar blue assay was performed (see Methods). Plates were read at dual wavelength (570 and 595 nm) in an ELISA plate reader.

those associated with imatinib. Because of its relative insolubility, WBZ_4 was incorporated into liposomes to promote cellular delivery (see Methods) (21). The proliferation of C-Kit–expressing GIST882 cells treated with WBZ_4 was markedly inhibited in a quantitative dose-dependent manner, similar to what occurred in imatinib-treated cells, with maximum impact at 1 μM bulk concentration (Figure 7A). By contrast, the inhibitory impact of WBZ_4 on CML K562 cells at the same bulk physiological dose of 1 μM is almost negligible (cell proliferation less than 10% lower than the proliferation of untreated cells), while 1 μM imatinib promotes a decrease in cell proliferation of approximately 66% (Figure 7B). These results demonstrate the higher specificity in anticancer activity of WBZ_4.

A Western blot assay on treated cancer-derived cell lines (Figure 8, A and B) was performed to determine the in-cell specificity of WBZ_4. The immunoblots revealed specificity toward C-Kit consistent with the selective anticancer activity on the GIST882 cell line that expresses C-Kit. Thus, the activating phosphorylation of C-Kit at sites Tyr703 and Tyr721 in ST882 cells is inhibited by WBZ_4 in a dose-sensitive manner as occurred in cells treated with imatinib (Figure 8A). By contrast, phosphorylation of Bcr-Abl at Tyr 412 (22) in K562 cells was not markedly inhibited (<15%) by WBZ_4, while densitometry revealed an imatinib-induced inhibition of approximately 85% (Figure 8B).

Since imatinib is a micromolar inhibitor of phosphorylated Bcr-Abl (Figure 5), the attack on CML cells at 1 μM bulk concentration (growth decrease 63%; Figure 7B) must be attributed to the inhibition of phosphorylated Bcr-Abl (Figure 8B) combined with the effective nanomolar inhibition of the unphosphorylated form (Figure 5). By contrast, WBZ_4 hinders the phosphorylation of Bcr-Abl only partially (Figure 8B), and in any case, it is an ineffective (micromolar) inhibitor of *both* forms of Bcr-Abl (Figure 5). Hence, its antitumor activity is predictably minimal on CML cells (Figure 7B). In the case of GIST cells, comparable antitumor activity of both compounds (Figure 7A) is likely to arise from comparable inhibitory impact (~85%; Figure 8A) on C-Kit phosphorylation and the fact that both compounds are nanomolar-affinity inhibitors of C-Kit (Figure 5).

Animal models: toward a selective GIST molecular therapy. To assay WBZ_4 for anticancer activity in vivo, an animal model for GIST growth based on female C.B-17/IcrHsd-*Prkdc*^{SCID} mice was developed de novo (see Methods). The model involved the subcutaneous injection of GIST882 cells (23). The efficacy of WBZ_4 was found to be comparable to that of imatinib, as determined by the decrease in tumor volume and weight (Figure 9, A and B). No obvious toxicities were observed in the animals during treatment, as determined by behavioral changes such as eating habits and mobility. Furthermore, mouse weights were not significantly different among the 3 groups of animals, suggesting that eating and drinking were not affected. Selectivity of WBZ_4 in the animal model using female C.B-17/IcrHsd-*Prkdc*^{SCID} mice was corroborated by assaying on the xenograft induced by CML cells K562

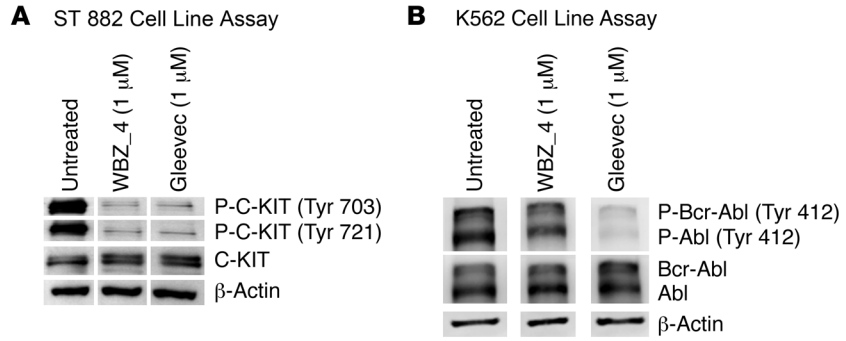

Figure 8
Higher specificity of WBZ_4 compared with imatinib as assayed through Western blots. (**A**) Western blot of C-Kit inhibition. WBZ_4 inhibits phosphorylation of C-Kit kinase in GIST882 cells. Gel bands from the Western blot assays (see Methods) of C-Kit and its phosphorylated form in GIST cells treated with WBZ_4 and imatinib. The β-actin assay was adopted as control. (**B**) Western blot of Bcr-Abl inhibition. Phosphorylation of Bcr-Abl kinase is not significantly inhibited by WBZ_4 in CML K562 cells. Electrophoretic gel bands for Western blots for Bcr-Abl kinase and its phosphorylated form in CML cells treated with WBZ_4 and imatinib.

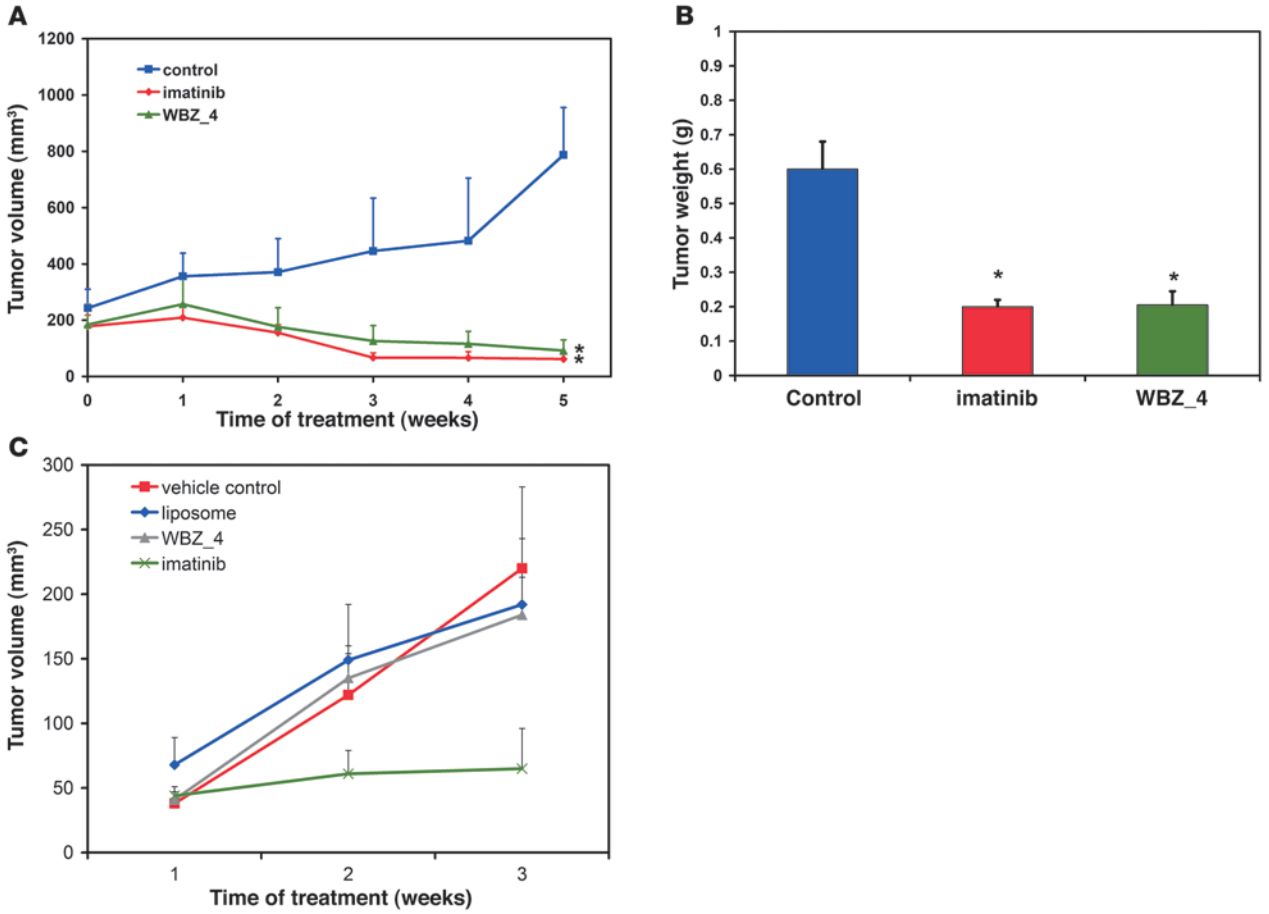

Figure 9

Xenograft models of anticancer activity. (**A**) Effect of WBZ_4 or imatinib therapy on in vivo GIST growth determined by longitudinal tumor volume measurements. Mice were randomized to treatment with either control (normal PBS and empty liposomes give indistinguishable results within experimental uncertainty), imatinib, or liposome-formulated WBZ_4. *$P < 0.01$. (**B**) Effect of WBZ_4 or imatinib therapy on in vivo GIST growth determined by weight measurements. Animals from all groups were sacrificed after 6 weeks of therapy, tumors were excised, and the weight was recorded. *$P < 0.05$. (**C**) Effect of WBZ_4 or imatinib therapy on in vivo CML growth induced through a xenograft of K562 tumor cells, determined by longitudinal tumor volume measurement. These results corroborate in vivo the in vitro finding of WBZ_4 selectivity.

(Figure 9C). While imatinib is shown to significantly impair tumor growth ($P < 0.01$), the prototype WBZ_4 has virtually no effect, in accordance with its engineered specificity and hence lack of inhibitory impact on Bcr-Abl kinase.

Cardiotoxicity in mice. As previously noted, studies of imatinib-induced cardiotoxicity identified a protective JNK (JNK1) inhibition as a means to reduce the collapse of mitochondrial membrane potential (15). Thus, WBZ_4 was engineered to inhibit JNK, a feature preliminarily corroborated in vitro (Figure 4). This protective role of WBZ_4 was also validated in vivo. Western blotting of cell extracts derived from the same imatinib- and WBZ_4-treated cardiomyocytes (see Methods) (Figure 10A) revealed that both drugs increased the phosphorylation state of ERK1/2 and $p38^{MAPK}$ as compared with untreated cultures. In contrast, cells treated with WBZ_4 showed reduced levels of JNK1/2 activation at each concentration tested, as compared with untreated cells or cells treated with imatinib. Our results confirm the recent observations of Kerkelä et al. (15) demonstrating that imatinib induces the ER stress response and activates JNKs in neonatal rat ventricular myocytes (NRVMs). JNK activation has been clearly associated with cardiomyocyte apoptosis via collapse of the mitochondrial membrane potential and release of cytochrome *c* (24). We further confirm that imatinib (and WBZ_4) had little effect on $p38^{MAPK}$ activation at concentrations below 50 μM and actually increased ERK activation in these cultured cells. In contrast, WBZ_4 appeared to reduce levels of pJNK1/2 at each dose tested, suggesting that upstream activation of JNKs was inhibited by WBZ_4. Thus, a direct inhibitory effect on JNK activity would predict that WBZ_4 should have reduced cardiotoxicity in vivo. This expectation is indeed supported by our observations using the surrogate marker brain natriuretic peptide (*BNP*), a most sensitive indicator of myocardial hypertrophy and cardiac impairment (25).

The expected curbing of cardiotoxicity in WBZ_4 anticancer therapy was confirmed by examining the mRNA levels of BNP in the left ventricle of mice from the same groups assayed for anticancer activity. The *BNP* mRNA levels were about 58% higher in the ventricles from imatinib-treated animals (Figure 10B), while no significant difference was detected in the WBZ_4-treated animals when compared with untreated mice. Finally, the reduced cardiotoxicity of WBZ_4 was directly tested in mice by determination of

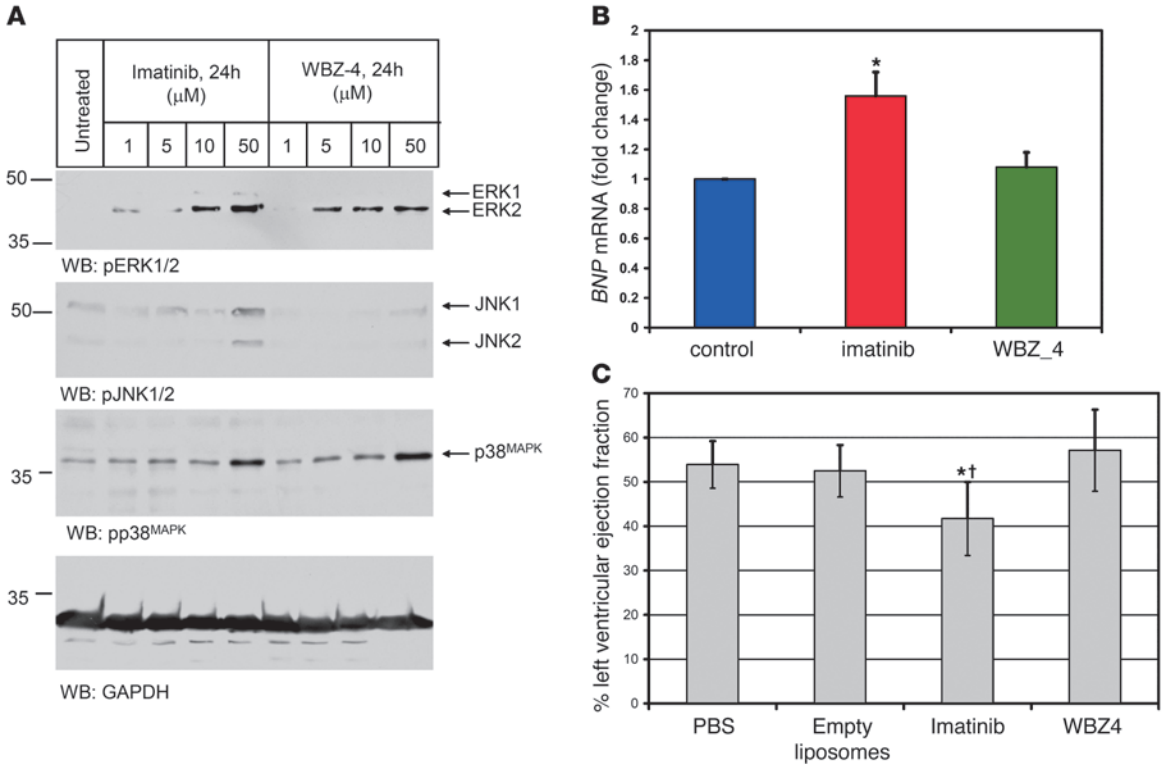

Figure 10
In vivo assays for cardiotoxicity of imatinib and WBZ_4. (**A**) Western blot of JNK inhibition in cardiomyocytes. Equal amounts of extracted cellular protein (50 μg per lane) were separated by SDS-PAGE and transferred to nitrocellulose membranes. Western blots were then probed with primary antibodies specific to the phosphorylated forms of ERKs, JNKs, and p38^{MAPK}. To ensure equal loading, blots were also probed with an antibody specific to GAPDH. The position of molecular weight standards is indicated to the left of each blot. (**B**) Effect of WBZ_4 or imatinib therapy on mouse heart *BNP*. The mRNA levels of *BNP* (a sensitive marker of myocardial hypertrophy and cardiac impairment) were examined in the left ventricle of mice from the groups in Figure 9A. The *BNP* mRNA levels were about 58% higher in the ventricles from imatinib-treated animals (*P = 0.02), but no significant difference was noted in the WBZ_4-treated animals. (**C**) Comparison of left-ventricular EF after 6 weeks of control (groups treated with either PBS or empty liposomes), imatinib, or WBZ_4 therapy in mice (doses are described in Methods). *P = 0.02 compared with PBS or empty liposomes; †P < 0.01 compared with WBZ_4.

the percentage ejection fraction (EF) in the left ventricle by MRI of treated mice subjected to imatinib or WBZ_4 therapy (Figure 10C). Following 6 weeks of therapy, the cardiac EF was significantly lower in the imatinib group compared with controls (P = 0.02), which is consistent with previous findings (15). Remarkably, WBZ_4 treatment had no effect on cardiac EF despite prolonged therapy (Figure 10C).

Discussion

We have modulated inhibitory impact by rationally reengineering imatinib motivated by the need to selectively inhibit the C-Kit kinase and curb imatinib cardiotoxicity. Since originally reported (15), this crucial side effect of imatinib has been a subject of some controversy (26). Our own in vivo and animal model assays corroborate the original findings and inspired our reengineering strategy. The discrepancy with the alternative study presented in ref. 26 is due to the fact that the latter is not a prospective one, as patients did not have baseline functional studies.

Our bottom-up approach is centered in a rational ligand redesign sculpting discriminating molecular features of the targets, i.e., their nonconserved dehydration propensities. Consequently, the redesign had 3 basic goals: (a) to refocus the primary impact on C-Kit kinase; (b) to reduce the inhibitory impact on Bcr-Abl kinase; and (c) to promote JNK inhibition in order to reduce cardiotoxicity. The 3 basic goals have been achieved, as attested by in vitro and in vivo results. The imatinib redesign turned our ligand into a selective prototherapeutic agent to treat GIST with a prima facie curbing of cardiotoxicity. A combination of in silico, in vitro, and cellular assays and animal testing validates our rational design strategy to refocus inhibitory impact based on the novel target discriminator.

Methods

Calculation of local dehydration propensities. We introduce a descriptor of hydration tightness for soluble proteins defined as the mean residence time of hydrating molecules within a domain around each residue on the protein surface. The local mean residence time, $\langle\tau\rangle_i$, of hydrating molecules at residue i is defined with respect to a spherical domain, $D(i)$, of 6.2-Å radius (approximate width of 3 water layers) (17) centered at the α-carbon of residue i. The actual computation of residence times is given in Supplemental Data. The mean residence times were obtained from classical trajectories generated by molecular dynamics simulations.

Backbone exposure for protein targets. The extent of backbone exposure at a particular residue was determined by counting the number of nonpolar side-chain groups contained within a 6.2-Å radius sphere (approxi-

mate thickness of 3 water layers) centered at the α-carbon. The extent of backbone shielding, η, in structured regions averaged over a nonredundant curated PDB database (1,662 proteins) is $\eta = 14.2$, with Gaussian dispersion of 8.2. Thus, a backbone site is regarded as exposed if the region is structurally disordered or $\eta < 6$. The statistics vary for desolvation radius in the range $6\ \text{Å} < r < 7\ \text{Å}$, but the tails of the distribution identify the same sites of backbone exposure. The structural integrity of soluble proteins requires that most backbone amides and carbonyls be protected from hydration. Thus, residues with absent backbone coordinates in a PDB entry are regarded as exposed and so are residues from natively disordered proteins.

Molecular dynamics simulations of protein-ligand interactions. The stochastic boundary molecular dynamics (SBMD) method (27) was employed to reduce simulation times while capturing localized interactions at the protein active site. The simulation were performed using the CHARMM program (28). Polar-hydrogen potential function (PARAM19) (29) was adopted for the protein, and a modified TIP3P water model (30) was used for the solvent. Partial charges on the kinase were computed by ab initio quantum calculation, and the van der Waals parameters of its atoms were adopted from amino acid side chains subsumed in the CHARMM force field. The system had a reaction zone and a reservoir region, and the reaction zone was further separated into a reaction region and a buffer region (28). Further details are provided in Supplemental Data.

Synthesis of prototype compound. The total synthesis of WBZ_4 (*N*-{5-[4-(4-methyl piperazine methyl)-benzoylamido]-2-methylphenyl}-4-[3-(4-methyl)-pyridyl]-2-pyrimidine amine) is described in Supplemental Data.

Liposomal incorporation of WBZ_4. WBZ_4 is under 10% water soluble. To promote cellular delivery, it was incorporated into liposomes that serve as drug carriers (21). WBZ_4 dissolved in DMSO was added to 1,2-dimyristoyl-*sn*-glycero-3-phosphocholine (DMPC) (Avanti) at 1:10 wt/wt drug/lipid ratio in the presence of excess *tert*-butanol. Tween-20 was added to the mixture in a 1:19 ratio of Tween-20 to WBZ_4/DMPC. The mixture was vortexed, frozen in an acetone/dry ice bath, and lyophilized. Before adding to cell cultures, this lyophilizate was reconstituted with normal 0.9% NaCl solution.

Cell proliferation assays. GIST cancer cells ST882 (8×10^3 cells per well) and CML cells K562 (1×10^4 cells per well) were seeded in 96-well plates in 100 μl of RPMI-1640 medium supplemented with 10% FBS and cultured for 24 hours. Cells were treated for 48 hours with 0.01, 0.1, and 1 μM/ml WBZ_4 and imatinib. Cell proliferation was determined by alamarBlue assay (BioSource; Invitrogen). Following 48 hours of exposure, 50 μl of medium was removed from each well and placed into a new 96-well plate. To reach a final volume of 100 μl per well, 40 μl of fresh medium and 10 μl of Alamar blue probe were added. Plates were read at dual wavelength (570 and 595 nm) in an ELISA plate reader (Kinetic Microplate Reader; Molecular Devices Corp.).

Western blots: inhibition of C-Kit phosphorylation in GIST cells. GIST882 cells were plated at 2.5×10^5 cells/well in 6-well plates in RPMI-1640 medium supplemented with 10% FBS. After allowing the cells to attach for 24 hours, the cells were treated with 1 μM of WBZ_4 or imatinib for 6 hours. For Western blotting, 50 μg of total protein was separated on a SDS-PAGE (Bio-Rad) and blotted onto nitrocellulose membranes (Life Science Research; Bio-Rad). Antibodies used were: anti–phospho–c-Kit polyclonal antibody, Tyr703 and Tyr721 (Zymed Laboratories Inc.), anti–c-Kit monoclonal antibody (E-1): sc-17806 (Santa Cruz Biotechnology Inc.), and anti–β-actin monoclonal antibody (Sigma-Aldrich).

Western blots: inhibition of Bcr-Abl phosphorylation in CML cells. K562 cells were plated at 5×10^5 cells/well. Two hours later, the cells were treated for 6 hours with 1 μM WBZ_4 or imatinib. Antibodies used were: anti–phospho–c-Abl (Tyr 412) monoclonal antibody 247C7 (Cell Signaling Technology Inc.) and anti-Abl monoclonal antibody (Sigma-Aldrich).

Kinetic spectrophotometric assays. To determine the enhancement of specificity of WBZ_4 relative to imatinib, kinetic assays of the inhibition of the Bcr-Abl and C-Kit kinase were conducted. The rate of phosphorylation due to kinase activity in the presence of inhibitors was spectrophotometrically assayed (11, 21): the ADP production was coupled to the NADH oxidation and determined by absorbance reduction at 340 nm. Reactions were carried out at 35°C in 500 μl of buffer (100 mM Tris-HCl, 10 mM $MgCl_2$, 0.75 mM ATP, 1 mM phosphoenol pyruvate, 0.33 mM NADH, 95 U/ml pyruvate kinase, pH 7.5). Autophosphorylation of the kinase is slow, requiring traces of hematopoietic cell kinase (Hck) to catalyze phosphorylation at sites Tyr393 and Tyr412. The reactant concentrations are 10 nM (Bcr-Abl), 12 nM (C-Kit), $[ATP]_o = 10$ mM, and $[\text{phosphorylation substrate}]_o = 0.5$ mM, where the subscripted "o" signifies "initial." The adopted peptide substrates (Invitrogen) for kinase phosphorylation are: EAIYAAPFAKKK for Tyr412-phosphorylated Bcr-Abl (19, 20); AEEEIYGEFEAKKKKG for unphosphorylated Brc-Abl (8, 19, 20); and KVVEEINGNNYVYIDPTQLPY for Tyr703/Tyr721-phosphorylated C-Kit (31).

In vitro colorimetric assays for kinase inhibition. Phosphorylation assays of antienzymatic activity of imatinib and WBZ_4 against Abl enzyme and C-Kit kinase were performed. The biotinylated substrate peptide [25 μM Abl-tide for Abl or 150 nM Poly(Glu4-Tyr) for C-Kit] in 100 mM sodium bicarbonate buffer (pH 8.0) was coated onto 96-well plates by incubation for 1 hour at room temperature. Subsequently, nonspecific binding sites were blocked by incubation with 3% BSA for 1 hour. Phosphorylation of peptide in 96-well plates was initiated by adding 10 ng Abl or 25 ng C-Kit in assay buffer (20 mM Tris, pH 7.4, 10 mM $MgCl_2$, 1 mM $MnCl_2$, 0.2 mM ATP, 1 mM dithiothretiol, 25 mM β-glycerol phosphate, 1 mM sodium orthovanadate, 5 mM EGTA). Different concentrations of drug inhibitors were added simultaneously to the wells and incubated for 1 hour at 37°C. Anti–phospho–Abl-tide or anti-phosphotyrosine and anti-rabbit antibodies (dilution 1:1,000) were incubated, in consecutive order, for 1 hour at room temperature. The chromophore reaction was initiated by adding 3,3′,5,5′-tetramethylbenzidene (TMB), and absorbance at 450 nm was measured 10 minutes later. Working volume was 100 μl (300 μl for BSA). Washing procedure (5 × 300 μl PBS) was performed after each step. Materials included: anti–phospho–Abl-tide (rabbit, polyclonal; Upstate), anti-phosphotyrosine (rabbit, polyclonal; Upstate), and anti-rabbit (HRP conjugate; Upstate) antibodies; Abl, Abl-tide (biotin conjugate; Upstate), c-Kit, Poly(Glu4-Tyr) (biotin conjugate; Upstate), TMB (Pierce Biotechnology), 96-well plates (streptavidin-coated) (Nunc), and plate reader (Tecan).

Animal models. All animal studies were approved by the Institutional Animal Care and Utilization Committee, University of Texas MD Anderson Cancer Center. Female C.B-17/IcrHsd-*Prkdc*^{SCID} mice were purchased from Harlan Sprague Dawley Inc. and housed in facilities approved by and in accordance with the American Association for Assessment and Accreditation of Laboratory Animal Care, the United States Department of Agriculture, the United States Department of Health and Human Services, and the NIH. Mice were used according to institutional guidelines when they were 8–12 weeks of age. GIST882 cells (23) were harvested from subconfluent cultures by a brief exposure to 0.25% trypsin-EDTA (Invitrogen). Trypsinization was stopped with medium containing 10% FBS. The cells were then washed twice in serum-free medium and resuspended in serum-free HBSS (Invitrogen). Single-cell suspensions with greater than 95% viability, as determined by Trypan blue exclusion, were used for the injections. To produce tumors, 6×10^6 GIST882 cells per 100 μl were injected subcutaneously into the unilateral flank of each SCID mouse. Five mice per group in the vehicle and imatinib groups and 7 mice in the WBZ_4 group were used. Once tumors were palpable (11 weeks from injection), mice were started on therapy with daily intraperitoneal injections of normal saline (vehicle),

imatinib (50 mg/kg), or liposomal WBZ_4 (50 mg/kg). Treatment was continued for 6 weeks, with weekly 2-dimensional measurements of tumor size. All mice were sacrificed when the tumor size approached 1.5 cm in the control group. Tumors were collected, fixed in formalin, and analyzed by H&E staining. Representative images were taken from each tumor using a light microscope at ×40 and ×100 magnification.

For the K562 model, tumor cells were collected from subconfluent suspensions, as described above. To produce tumors, 10×10^6 K562 cells per 100 μl were injected subcutaneously into the unilateral flank of each SCID mouse. Once tumors were palpable (2 weeks after injection), the mice were then randomized into the following groups ($n = 7$ per group): (a) normal saline daily; (b) empty liposomes daily; (c) imatinib (doses listed above); and (d) WBZ_4 (doses listed above). Treatment continued until mice in any of the groups developed large tumor burden, at which point all animals were sacrificed. Tumors were measured weekly during treatment and at necropsy.

Liposomal WBZ_4 preparation for in vivo testing. In excess *tert*-butanol (Sigma-Aldrich), WBZ_4 and DMPC (Avanti Polar Lipids Inc.) were mixed in a 1:10 molar concentration. Tween-20 (Sigma-Aldrich) was also added to the mixture. Following a quick freeze in a dry ice–acetone water bath, the mixture was lyophilized for 24 hours. The liposomes were stored at –20°C until ready to use. Immediately before each treatment, the liposomes were reconstituted in normal saline.

Cardiomyocyte cell culture experiments: reagents. PC-1 tissue culture medium was from BioWhittaker. DMEM was purchased from GIBCO-BRL (Invitrogen), type II collagenase from Worthington, and penicillin-streptomycin from Fisher Scientific/MediaTech. Phospho-specific ERK and JNK polyclonal antibodies were from Promega, and phospho-specific $p38^{MAPK}$ polyclonal antibody was from Cell Signaling. GAPDH monoclonal antibody was from Novus Biologicals. SuperSignal West Pico chemiluminescent substrate was obtained from Pierce Biotechnology. All other reagents were from Sigma-Aldrich or Baxter S/P.

Cardiomyocyte cell culture experiments: NRVM isolation. Animals used in these experiments were handled in accordance with the *Guide for the care and use of laboratory animals* (NIH publication no. 85-23. Revised 1985). NRVMs were isolated from the hearts of 2-day-old Sprague-Dawley rat pups via collagenase digestion as previously described (32). Dissociated cells were preplated for 1 hour in serum-free PC-1 medium to selectively remove non-muscle cells. Myocytes were then plated in PC-1 medium at a density of 1,600 cells/mm^2 onto collagen-coated, 35-mm plastic dishes and left undisturbed in a 5% CO_2 incubator for 24 hours. Unattached cells were removed by aspiration, and the attached cells were maintained in a solution of DMEM/Medium 199 (4:1) containing antibiotic/antimycotic solution for 24 hours. Thereafter, cells were maintained in control medium or treated with imatinib or WBZ_4 (1–50 μM; 24 hours).

Cardiomyocyte cell culture experiments: Western blotting. NRVMs were homogenized in lysis buffer (33). Equal amounts of extracted proteins were separated on 10% SDS-polyacrylamide gels with 5% stacking gels. Proteins were transferred to nitrocellulose membranes and the Western blots probed with antibodies specific to the phosphorylated forms of ERKs, JNKs, or $p38^{MAPK}$. To ensure equal loading, membranes were also probed with an antibody specific to GAPDH. Primary antibody binding was detected with HRP-conjugated goat anti-mouse or goat anti-rabbit secondary antibody, and visualized by enhanced chemiluminescence.

MRI and assessment of cardiac function. Assessment of left-ventricular function was performed as previously described (34). In brief, representative in vivo axial images of the left ventricle in diastole and systole of control and test mice were acquired in a 4.7T MR scanner cardiac gating using a magnetization-prepared spoiled gradient echo sequence. To assess cardiac function, short axis cardiac cine images were acquired using a magnetization-prepared, cardiac-gated spoiled gradient echo sequence (TE/TR 2.1 ms/~23.5 ms; 16 phases covering 1.5 R-R cycles; in-plane resolution 312 μm × 312 μm; 1.25-mm slice thickness). For assessment of EF, regions of interest encompassing the cavity of the left ventricle were drawn. For each animal, the average region of interest of 4 central slices in systole was divided by the average region of interest of 4 central slices in diastole taken at the same location in the left ventricle to derive the EF.

Cardiotoxicity/RT-PCR analysis. Total RNA was extracted from mouse heart samples using the RNeasy kit (QIAGEN) according to the manufacturer's instructions. The mRNA levels of *BNP* were examined in the left ventricle of mice from the GIST animal model groups treated exclusively with either WBZ_4 or imatinib. The RT-PCR was performed as described previously (34). The primer sequences were as follows: *BNP*, 5′-AGCTGCTGGAGCTGATAAGA-3′ (fwd) and 5′-TTACAGCCCAAACGACTGAC-3′ (rev) (24); β-actin, 5′-ATCTGGCACCACACCTTCTACA-ATGA-3′ (fwd) and 5′-CGTCATACTCCTGCTTGCTGATCCAC-3′ (rev).

Statistical analysis for in vivo tests. Continuous variables were compared with either the Student's *t* test or ANOVA. Prior to analysis, all distributions were examined for outliers and non-normality. If appropriate, nonparametric tests (Mann-Whitney *U* test) were utilized to compare differences. All statistical analyses were performed with SPSS software. $P < 0.05$ was considered statistically significant.

Acknowledgments

The research of A. Fernández was supported by NIH grant R01 GM072614 and by a grant from the Gulf Coast Center for Computational Cancer Research. J. Ma acknowledges support from the Welch Foundation. G. Lopez-Berestein acknowledges support from CA. A.K. Sood acknowledges support from the University of Texas MD Anderson Cancer Center SPORE in ovarian cancer (P50CA83639) and a Program Project Development Grant from the Ovarian Cancer Research Fund Inc. The GIST882 cells were a gift from Jonathan Fletcher, Dana-Farber Cancer Institute–Harvard Medical School.

Received for publication April 11, 2007, and accepted in revised form September 5, 2007.

Address correspondence to: Ariel Fernández, Department of Bioengeneering, Rice University, 6100 Main, MS 142, Houston, Texas 77005, USA. Phone: (713) 348-3681; Fax: (713) 348-3699; E-mail: arifer@rice.edu.

1. Dancey, J., and Sausville, E.A. 2003. Issues and progress with protein kinase inhibitors for cancer treatment. *Nat. Rev. Drug Discov.* **2**:296–313.
2. Levitski, A., and Gazit, A. 1995. Tyrosine kinase inhibition: an approach to drug development. *Science.* **267**:1782–1788.
3. Tibes, R., Trent, J., and Kurzrock, R. 2005. Tyrosine kinase inhibitors and the dawn of molecular cancer therapeutics. *Annu. Rev. Pharmacol. Toxicol.* **45**:357–384.
4. Gibbs, J., and Oliff, A. 1994. Pharmaceutical research in molecular oncology. *Cell.* **79**:193–198.
5. Donato, N.J., and Talpaz, M. 2000. Clinical use of tyrosine kinase inhibitors: therapy for chronic myelogenous leukemia and other cancers. *Clin. Cancer Res.* **6**:2965–2966.
6. Fabian, M.A., et al. 2005. A small molecule kinase interaction map for clinical kinase inhibitors. *Nat. Biotechnol.* **23**:329–336.
7. Gambacorti-Passerini, C., et al. 1997. Inhibition of the ABL kinase activity blocks the proliferation of BCR/ABL+ leukemic cells and induces apoptosis. *Blood Cells Mol. Dis.* **23**:380–394.
8. Schindler, T., et al. 2000. Structural mechanism for STI-571 inhibition of Abelson tyrosine kinase. *Science.* **289**:1938–1942.
9. Attoub, S., et al. 2002. The c-kit tyrosine kinase inhibitor STI-571 for colorectal cancer therapy. *Cancer Res.* **62**:4879–4883.
10. DeMatteo, R.P. 2002. The GIST of targeted cancer therapy: a tumor (gastrointestinal stromal tumor), a mutated gene (c-kit), and a molecular inhibitor (STI571). *Ann. Surg. Oncol.* **9**:831–839.

11. Skene, R.J., et al. 2004. Structural basis for autoinhibition and STI-571 inhibition of C-kit Tyrosine kinase. *J. Biol. Chem.* **279**:31655–31663.
12. Tuveson, D.A., et al. 2001. STI571 inactivation of the gastrointestinal stromal tumor c-Kit oncoprotein: biological and clinical implications. *Oncogene.* **20**:5054–5058.
13. Chen, J.P., Zhang, X., and Fernández, A. 2007. Molecular basis for specificity in the druggable kinome: sequence-based analysis. *Bioinformatics.* **23**:563–572.
14. Knight, Z.A., and Shokat, K.M. 2005. Features of selective kinase inhibitors. *Chem. Biol.* **12**:621–637.
15. Kerkela, R., et al. 2006. Cardiotoxicity of the cancer therapeutic agent imatinib mesylate. *Nat. Med.* **12**:908–916.
16. Druker, B.J. 2004. Molecularly targeted therapy: have the floodgates opened? *Oncologist.* **9**:357–360.
17. Fernández, A., and Scheraga, H.A. 2003. Insufficiently dehydrated hydrogen bonds as determinants of protein interactions. *Proc. Natl. Acad. Sci. U. S. A.* **100**:113–118.
18. Barker, S., et al. 1995. Characterization of $pp^{60c\text{-}src}$ tyrosine kinase activities using a continuous assay: autoactivation of the enzyme is an intermolecular autophosphorylation process. *Biochemistry.* **34**:14843–14851.
19. Songyang, Z., et al. 1995. Catalytic specificity of protein-tyrosine kinases is critical for selective signalling. *Nature.* **373**:536–539.
20. Clarkson, B., Strife, A., Wisniewski, D., Lambek, C.L. and Liu, C. 2003. Chronic myelogenous leukemia as a paradigm of early cancer and possible curative strategy. *Leukemia.* **17**:1211–1262.
21. Estey, E.H., et al. 1999. Molecular remissions induced by liposomal-encapsulated all-trans retinoic acid in newly diagnosed acute promyelocytic leukemia. *Blood.* **94**:2230–2235.
22. Dorey, K, et al. 2001. Phosphorylation and structure-based functional studies reveal a positive and a negative role for the activation loop of the c-Abl tyrosine kinase. *Oncogene.* **20**:8075–8081.
23. Prenen, H., Deroose, C., Vermaelen, P., Sciot, R., and Debiec-Rychter, M. 2006. Establishment of a mouse gastrointestinal stromal tumour model and evaluation of response to Imatinib by small animal positron emission tomography. *Anticancer Res.* **26**:1247–1252.
24. Baines, C.P., and Molkentin, J.D. 2005. Stress signaling pathways that modulate cardiac myocyte apoptosis. *J. Mol. Cell. Cardiol.* **38**:47–62.
25. Scheuermann-Freestone, M., et al. 2001. A new model of congestive heart failure in the mouse due to chronic volume overload. *Eur. J. Heart Fail.* **3**:535–543.
26. Verweij, J., et al. 2007. Imatinib does not induce cardiac left ventricular failure in gastrointestinal stromal tumours patients: analysis of EORTC-ISG-AGITG study 62005. *Eur. J. Cancer.* **43**:974–978.
27. Brooks, C.L., III, and Karplus, M. 1989. Solvent effects on protein motion and protein effects on solvent motion: dynamics of the active site region of lysozyme. *J. Mol. Biol.* **208**:159–181.
28. Brooks, B.R. 1983. CHARMM: a program for macromolecular energy, minimization, and dynamics calculations. *J. Comput. Chem.* **4**:187–217.
29. Neria, E., Fischer, S., and Karplus, M. 1996. Simulation of activation free energies in molecular systems. *J. Chem. Phys.* **105**:1902–1921.
30. Jorgensen, W.L. 1981. Transferable intermolecular potential functions for water, alcohols, and ethers. Application to liquid water. *J. Am. Chem. Soc.* **103**:335–340.
31. Timokhina, I., Kissel, H., Stella, G., and Besmer, P. 1998. Kit signaling through PI 3-kinase and Src kinase pathways: an essential role for Rac1 and JNK activation in mast cell proliferation. *EMBO J.* **17**:6250–6262.
32. Samarel, A.M., and Engelmann, G.L. 1991. Contractile activity modulates myosin heavy chain-β expression in neonatal rat heart cells. *Am. J. Physiol.* **261**:H1067–H1077.
33. Schlaepfer, D.D., and Hunter, T. 1996. Evidence for in vivo phosphorylation of the Grb2 SH2-domain binding site on focal adhesion kinase by Src-family protein-tyrosine kinases. *Mol. Cell. Biol.* **16**:5623–5633.
34. Thaker, P.H., et al. 2006. Chronic stress promotes tumor growth and angiogenesis in a mouse model of ovarian carcinoma. *Nat. Med.* **12**:939–944.